AGU PUBLICATIONS

JGR

Journal of Geophysical Research: Planets

RESEARCH ARTICLE

10.1002/2013JE004482

Key Points:
- New impact craters expose ground ice at high latitudes on Mars
- Ice is found at latitudes as low as 39°N
- Ice remains visible for many months, indicating low regolith content

Supporting Information:
- Readme
- Animation S1

Correspondence to:
Colin M. Dundas,
cdundas@usgs.gov

Citation:
Dundas, C. M., S. Byrne, A. S. McEwen, M. T. Mellon, M. R. Kennedy, I. J. Daubar, and L. Saper (2014), HiRISE observations of new impact craters exposing Martian ground ice, *J. Geophys. Res. Planets*, *119*, 109–127, doi:10.1002/2013JE004482.

Received 8 JUL 2013
Accepted 18 DEC 2013
Accepted article online 23 DEC 2013
Published online 27 JAN 2014

HiRISE observations of new impact craters exposing Martian ground ice

Colin M. Dundas[1], Shane Byrne[2], Alfred S. McEwen[2], Michael T. Mellon[3], Megan R. Kennedy[4], Ingrid J. Daubar[2], and Lee Saper[4]

[1]Astrogeology Science Center, U. S. Geological Survey, Flagstaff, Arizona, USA, [2]Lunar and Planetary Laboratory, University of Arizona, Tucson, Arizona, USA, [3]Southwest Research Institute, Boulder, Colorado, USA, [4]Malin Space Science Systems, San Diego, California, USA

Abstract Twenty small new impact craters or clusters have been observed to excavate bright material inferred to be ice at mid-latitudes and high latitudes on Mars. In the northern hemisphere, the craters are widely distributed geographically and occur at latitudes as low as 39°N. Stability modeling suggests that this ice distribution requires a long-term average atmospheric water vapor content around 25 precipitable micrometers, more than double the present value, which is consistent with the expected effect of recent orbital variations. Alternatively, near-surface humidity could be higher than expected for current column abundances if water vapor is not well mixed with atmospheric CO_2, or the vapor pressure at the ice table could be lower due to salts. Ice in and around the craters remains visibly bright for months to years, indicating that it is clean ice rather than ice-cemented regolith. Although some clean ice may be produced by the impact process, it is likely that the original ground ice was excess ice (exceeding dry soil pore space) in many cases. Observations of the craters suggest small-scale heterogeneities in this excess ice. The origin of such ice is uncertain. Ice lens formation by migration of thin films of liquid is most consistent with local heterogeneity in ice content and common surface boulders, but in some cases, nearby thermokarst landforms suggest large amounts of excess ice that may be best explained by a degraded ice sheet.

1. Introduction

Recent orbital imaging of Mars has revealed new impact craters formed within the period of spacecraft observation. Beginning with discoveries by the Mars Orbiter Camera (MOC) [*Malin et al*., 2006] and continuing with the Mars Reconnaissance Orbiter (MRO) cameras, over 200 new craters or crater clusters have been observed [*Daubar et al*., 2013]. Most of the known craters are concentrated in low-latitude dusty regions, where they are highlighted by relatively dark blast patterns that are much larger than the craters. The discovery of these impacts exposing ice at mid-latitudes and high latitudes [*Byrne et al*., 2009] has opened a new avenue for the study of Martian ground ice.

The global distribution of shallow ground ice on Mars is now well understood in general terms. In the course of a study of Mars' polar caps, *Leighton and Murray* [1966] presented a model for ice stability that has been refined by many subsequent studies, summarized by *Mellon et al*. [2008a]. Recent global maps of the distribution of conditions for stable ice have been produced by *Mellon et al*. [2004], *Schorghofer and Aharonson* [2005], and *Chamberlain and Boynton* [2007]. The basis of these models is the assumption that the ice table is in diffusive equilibrium with water vapor in the atmosphere. Ice is stable where temperatures are low enough that the annual average water vapor density at the ice table is equal to (or less than) that in the atmosphere, leading to no net transport (or deposition at the ice table). This model predicts that ice will be unstable at any depth near the equator but abruptly becomes stable beneath a desiccated layer poleward of some point in the mid-latitudes, currently around ±40–50°. Such a layer damps annual temperature fluctuations, reducing the average water vapor content at the ice table because the saturation vapor pressure has strongly nonlinear temperature dependence. The stability depth shallows toward the pole because lower average temperatures lead to a lower required thickness of dry soil.

The general picture that has emerged from these models has ice stable at a depth on the order of a meter at around 40–50° latitude, rapidly shallowing to centimeters near the poles. Observational support for such an ice distribution has been provided by Gamma Ray Spectrometer (GRS) results, although these have an

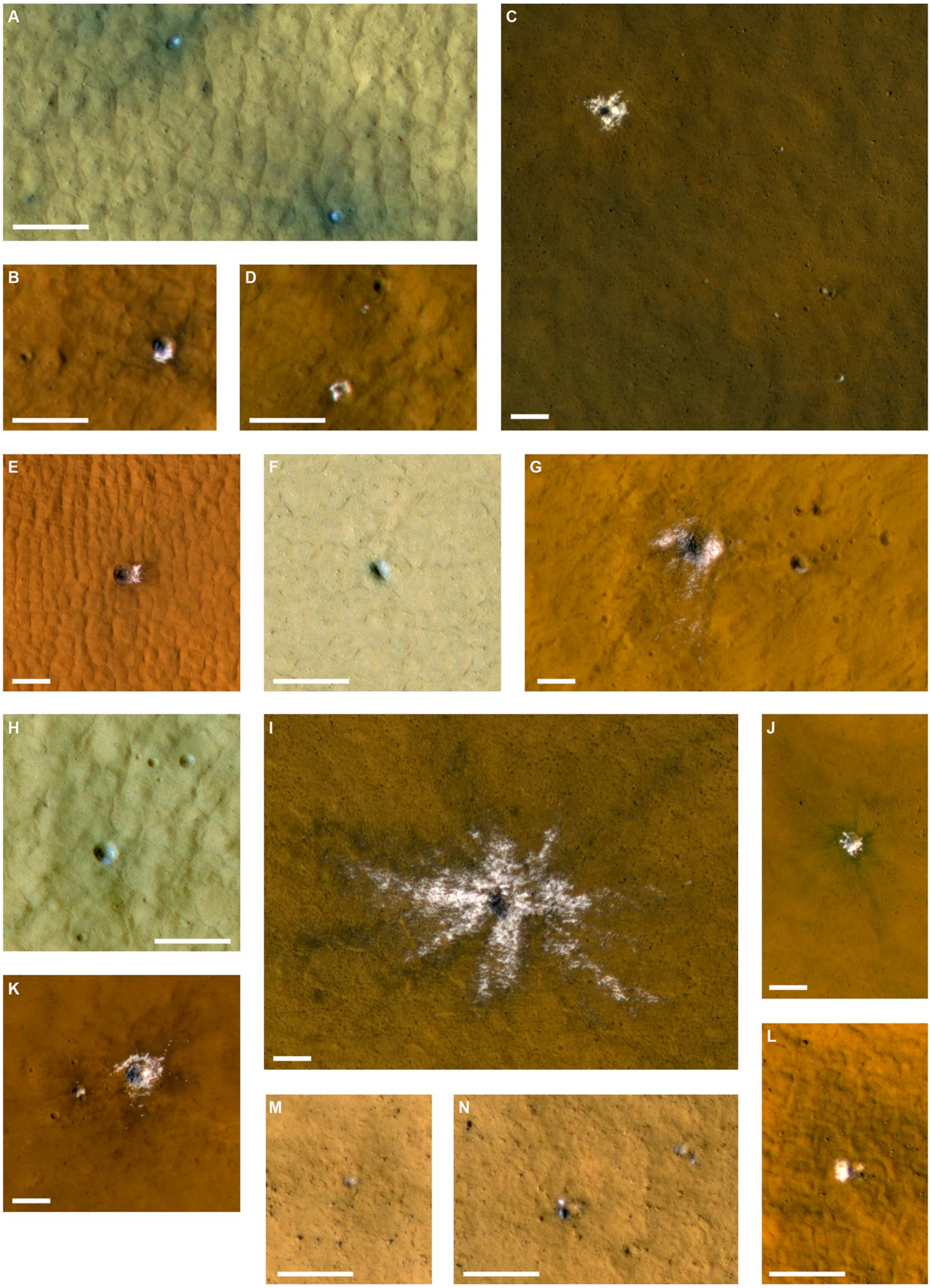

Figure 1. Cutouts of HiRISE images of ice-exposing impacts, illustrating the range of observed morphologies. (a) Site 1, PSP_009978_2265. (b) Site 2, PSP_0010440_2235. (c) Site 3, PSP_010625_2360. (d) Site 4, PSP_010585_2255. (e) Site 5, PSP_010861_2265. (f) Site 6, ESP_017530_2310. (g) Site 7, ESP_016954_2245. (h) Site 8, ESP_016994_2245. (i) Site 9, ESP_017868_2440. (j) Site 10, ESP_017789_2335. (k) Site 11, ESP_017926_2310. (l) Site 12, ESP_018125_2445. (m) and (n) Site 13, ESP_018573_2415. (o) Site 14, ESP_025840_2240. (p) Site 15, ESP_025642_2310. (q) Site 16, ESP_026802_2305. (r) Site 17, ESP_027000_2325. (s) Site 18, ESP_029467_2195. (t) Site 19, ESP_032118_1085. (u) Site 20, ESP_032340_1060. Scale bar for each cutout is 20 m. In most cases, the image shown is the initial HiRISE image, for which ice is most extensive. All images are individually stretched for contrast. Figures 1a–1s have north up and light from the (lower) left. Figures 1t and 1u are in polar stereographic projection. The original HiRISE images used in this study are available from the Planetary Data System or at http://hirise.lpl.arizona.edu. Credit for all HiRISE images: NASA/Jet Propulsion Laboratory (JPL)/University of Arizona.

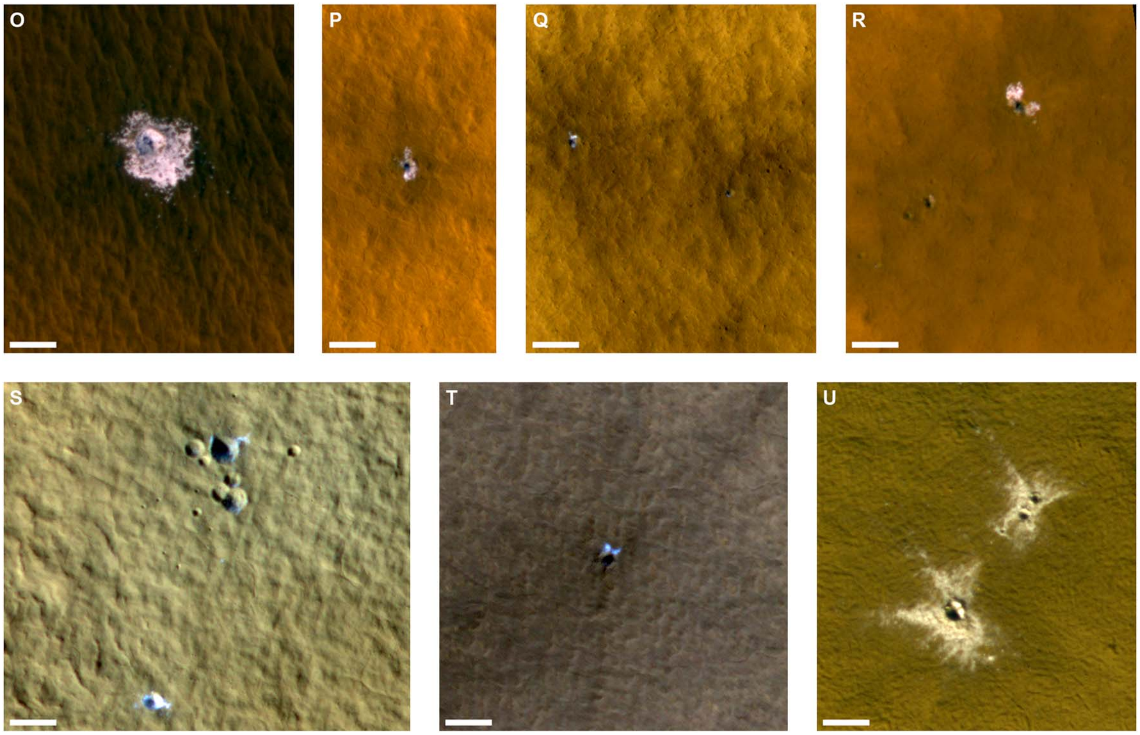

Figure 1. (continued)

effective resolution of only ~600 km [e.g., *Boynton et al*., 2002; *Mellon et al*., 2004; *Feldman et al*., 2008]. More recent support has come from the Phoenix Lander [*Mellon et al*., 2009] and Mars Advanced Radar for Subsurface and Ionospheric Sounding [*Mouginot et al*., 2010]. While models and observations broadly agree on the geographic distribution of ground ice, questions remain concerning the nature and origin of the ice and the processes that have shaped it.

Impact craters provide another probe of Martian ice (Figure 1). *Byrne et al*. [2009] reported the initial discovery of five new impact sites, where ice was exposed, all within a narrow band of longitude. They found that the latitudinal distribution of ice was consistent with models that assumed an atmospheric water content corresponding to a column abundance of ~20 precipitable micrometers (pr μm), somewhat higher than the present global average value. This might reflect the time scale for ice to adjust to changes in climate rather than any inadequacy of the theory, since the region of stability varies greatly with changes to Mars' orbit [*Mellon and Jakosky*, 1995], and ice was stable at lower latitudes in the northern hemisphere as recently as ~10 ka [*Chamberlain and Boynton*, 2007]. Modeling by *Byrne et al*. [2009] and *Dundas and Byrne* [2010] indicated that ice remained visible through intervals in which millimeters of ice sublimated, requiring that the ice be relatively clean rather than ice-cemented ground. *Kossacki et al*. [2011] modeled similar sublimated thicknesses but interpreted darkening as due to optical properties of the ice layer rather than a sublimation lag. They suggested that this was consistent with sublimation of a post impact coating of surface ice.

Since the publication of *Byrne et al*. [2009], 15 additional ice-exposing impact sites have been found. In this paper, we summarize an observing campaign by the High Resolution Imaging Science Experiment (HiRISE) [*McEwen et al*., 2007a] to characterize these sites. We discuss the global distribution and properties of these impact sites and changes to the sites over time. We then describe the periglacial geomorphology in the vicinity of the impacts and discuss the distribution and nature of the exposed ice.

2. Observing Campaign

Newly formed impact craters on Mars are generally first observed as dark spots in images by the Context Camera (CTX) [*Malin et al*., 2007] on the Mars Reconnaissance Orbiter (MRO) spacecraft (Figure 2). Discovery of

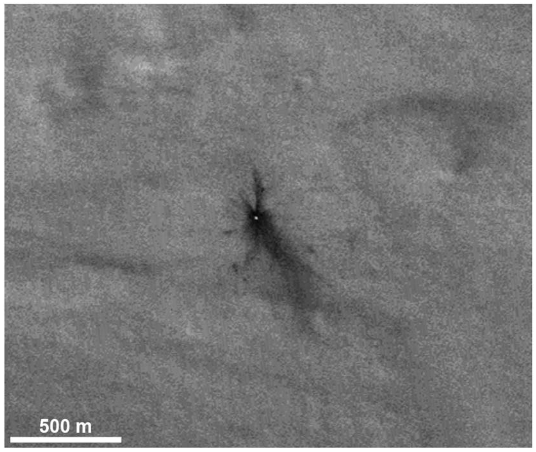

Figure 2. Example of a CTX discovery image, in this case for site 6. Note the dark ejecta and bright point at the center. (CTX image P18_008102_2285_XI_48N081W, stretched for maximum contrast. North is up. Image credit: NASA/JPL/Malin Space Science Systems.)

new impacts is strongly biased toward dusty locations, since it is the large dark blast zone rather than the crater itself that is initially observed [*Malin et al.*, 2006]. Where previous data from MOC, CTX, the Thermal Emission Imaging System (THEMIS) on Mars Odyssey [*Christensen et al.*, 2004], or the High Resolution Stereo Camera (HRSC) on Mars Express [*Neukum et al.*, 2004] cover the location, it is possible to determine whether the dark patch is new and constrain the date of its formation. In some cases (generally the largest impacts) when ice is exposed, CTX observes one or more bright pixels within the dark patch.

After initial discovery, dark patches are targeted for HiRISE follow-up imaging. At the time of writing, 20 ice-exposing impacts have been observed (Figure 1). Table 1 summarizes the basic parameters of each site, and Table 2 gives the constraints on the timing of formation. Figure 3 shows the geographic distribution of ice-exposing impacts. Six sites were discovered in the northern summer of Mars Year 29 (MY29), seven in MY30, and seven in MY31. (MY refers to the Mars calendar of *Clancy et al.* [2000], and this notation will be used throughout this paper; years begin at $L_S = 0°$, the beginning of northern spring. MY32 began on 31 July 2013.) Two of the MY31 sites are the first southern hemisphere ice exposures.

In order to monitor changes to the visible ice over time, we have repeatedly imaged these sites with the HiRISE camera, capable of observing at scales as small as 25–32 cm/pixel with high signal-to-noise ratio. Typical HiRISE observations are 5–6 km wide with a center swath (~1.2 km wide) acquired in three colors,

Table 1. Parameters of Icy Impact Sites

Site No.	Latitude[a]	Longitude[a]	Elevation (km)	Albedo[b]	Thermal Inertia[c]	Setting[d]	Largest Icy Crater Diameter (m)	Atm. Water (pr μm)[e]
18	39.11	190.25	−4.0	0.25	139	Plains near lobate debris aprons (LDAs)	12	25
2	43.29	164.21	−2.8	0.27	178	LDAs	6	19
14	43.9	204.35	−4.0	0.24	198	Plains	12.75	23
7	44.22	164.2	−2.7	0.27	184	Plains near LDAs	24	17
8	44.35	152.93	−3.7	0.27	189	Lobate crater ejecta	6.75	17
4	45.06	164.7	−2.8	0.26	169	LDAs/plains	4.5	15
5	46.18	188.5	−4.0	0.25	187	Plains	12	14
1	46.35	176.89	−4.0	0.24	233	LDAs/plains	4	18
16	50.37	219.71	−3.1	0.26	132	Crater fill	5.5	3
11	50.51	265.2	−0.7	0.23	142	Plains	14.75	5
6	50.67	278.4	−2.7	0.22	207	Plains near LDAs	5.75	8
15	50.78	208.76	−3.7	0.25	172	Plains	5.75	4
17	52.01	214.7	−3.3	0.26	138	Crater ejecta	8	2
10	53.27	46.26	−3.6	0.22	202	Plains	9	4
3	55.58	150.6	−4.1	0.15	261	Plains	8	4
13	60.99	238.72	−3.2	0.22	185	Plains	4.5	1
9	63.92	44.88	−4.3	0.20	256	Plains	20	1
12	64.29	231.5	−3.6	0.22	163	Plains	4	1
19	−71.5	191.53	0.9	0.20	75	Possible SPLD outlier	7	1
20	−73.69	250.63	1.4	0.18	124	Plains in crater	8.5	1

[a]Coordinates are planetocentric latitude and east longitude.
[b]Thermal Emission Spectrometer [*Christensen et al.*, 2001] bolometric albedo; median of 5 × 5 pixel region of 8 pixel/degree map.
[c]Nighttime thermal inertia from *Putzig and Mellon* [2007]; median of 5 × 5 pixel region of 20 pixel/degree map. Units are J m^{-2} K^{-1} s$^{-1/2}$ (tiu).
[d]LDAs are lobate debris aprons, which are very ice rich in many cases [*Holt et al.*, 2008; *Plaut et al.*, 2009]. LDAs/plains indicate craters in locally flat areas that may be merged LDAs. SPLD is the south polar layered deposits.
[e]Minimum atmospheric water content for stable ice, see section 3.2. The minimum value tested was 1 pr μm.

Table 2. Timing Constraints

Site	Last Before[a]	First After[a]	Dates (D/M/Y)	L_S/Mars Years[b]
1	P20_008699_2247	P22_009556_2263	4/6/2008 to 10/8/2008	81°/MY29–111°/MY29
2	V22273012	P21_009095_2225	22/12/2006 to 5/7/2008	154°/MY28–94°/MY29
3	V27128013	B01_010058_2375	26/1/2008 to 18/9/2008	23°/MY29–129°/MY29
4	V27090026	B01_010018_2247	22/1/2008 to 15/9/2008	21°/MY29–127°/MY29
5	V11315010	P20_009015_2262	3/7/2004 to 28/6/2008	55°/MY27–92°/MY29
6	H3305_0000_ND3	P18_008102_2285	6/8/2006 to 18/4/2008	89°/MY28–60°/MY29
7	V29124006	B17_016387_2256	8/7/2008 to 24/1/2010	96°/MY29–42°/MY30
8	V10530010	B17_016216_2244	29/4/2004 to 11/1/2010	26°/MY27–36°/MY30
9	V27868007	B19_017156_2424	26/3/2008 to 25/3/2010	50°/MY29–69°/MY30
10	V27194020	B20_017433_2324	31/1/2008 to 15/4/2010	25°/MY29–78°/MY30
11	V27124014	B20_017570_2311	25/1/2008 to 26/4/2010	22°/MY29–82°/MY30
12	V27874007	B21_017848_2426	27/3/2008 to 18/5/2010	50°/MY29–92°/MY30
13	V30469005	B21_018006_2414	27/10/2008 to 30/5/2010	148°/MY29–97°/MY30
14	V28611017	G19_025484_2254	27/5/2008 to 3/1/2012	77°/MY29–52°/MY31
15	?[c]	G15_023941_2310	?[c] to 5/9/2011	?[c]–356/MY30
16	B21_018007_2306	G21_026446_2327	30/5/2010 to 18/3/2012	97°/MY30–85°/MY31
17	V29584014	G22_026644_2316	15/8/2008 to 2/4/2012	113°/MY29–91°/MY31
18	D02_027845_2198[d]	D05_029045_2199	5/7/2012 to 23/10/2012	135°/MY31–193°/MY31
19	V15396003[e]	D12_031841_1075	4/6/2005[e] to 12/5/2013	224°/MY27[e]–317°/MY31
20	D12_031773_1061	D13_032129_1053	7/5/2013 to 4/6/2013	314°/MY31–330°/MY31

[a]Images used as timing constraints. THEMIS visible wavelength images have prefix V, CTX images have P and B, and HRSC images have H. CTX image IDs are abbreviated. Intervening images were omitted if considered unreliable constraints due to low resolution or low quality.
[b]Mars year uses the calendar of *Clancy et al.* [2000].
[c]No constraint available from medium- or high-resolution imagery. However, the preservation of the dark blast zone in HiRISE image ESP_025642_2310 strongly suggests that this crater postdates the seasonal cap from late MY30 (section 5.2).
[d]Image does not cover main cluster, but a secondary crater visible in the later CTX image is not visible in this image.
[e]Likely to be after the southern winter of MY31, since the blast pattern has not been reworked by the seasonal cap.

using blue-green (BG) and near-infrared (IR) filters as well as the wider-area red filter coverage. Due to the small size of the craters, observations were usually acquired without binning or with the BG and IR CCDs at bin 2 (50–60 cm/pixel). The craters were within the color swath of almost all images. Few observations were attempted during autumn and winter due to poor lighting and haze. Initial imaging in the spring of MY30 was delayed because MRO was in safe mode for an extended period between approximately $L_S = 328°$ of MY29 and $L_S = 24°$ of MY30; as a result, the first HiRISE image of site 6 was not acquired until early in MY30, despite initial discovery by CTX in MY29. This paper incorporates data through northern summer of MY31 for the northern hemisphere sites and southern summer of MY31 for the southern hemisphere sites.

Hyperspectral images from CRISM (Compact Reconnaissance Imaging Spectrometer for Mars) [*Murchie et al.*, 2007] have been acquired covering many of the craters at 18 m/pixel. One such observation was used by *Byrne et al.* [2009] to confirm that the bright material was indeed water ice. Because of the small sizes of the craters, such observations generally have at most a few CRISM pixels containing any ice. Additional CRISM observations of these craters have been described by *Cull et al.* [2012], who concluded that the spectra were consistent with relatively pure ice.

3. Global Distribution

3.1. Crater Observations

The northern hemisphere distribution of ice-exposing impacts accords well with the general nature of model predictions of the distribution of stable ice, confirming the interpretation of *Byrne et al.* [2009]. Ice is commonly observed in new impacts above 39°N and absent at lower latitudes. The longitudinal distribution is much more extensive than the distribution observed by *Byrne et al.* [2009]. Only three new impacts at high southern latitudes have been observed beyond the two reported by *Byrne et al.* [2009]. Two of the new craters are on the South Polar Layered Deposits (SPLD), but only one exposes visible ice. This is attributable to a lack of dusty surfaces at middle and high southern latitudes (Figure 3a), which leads to a marked detection bias. Apparent longitudinal variations in the northern hemisphere are probably due to

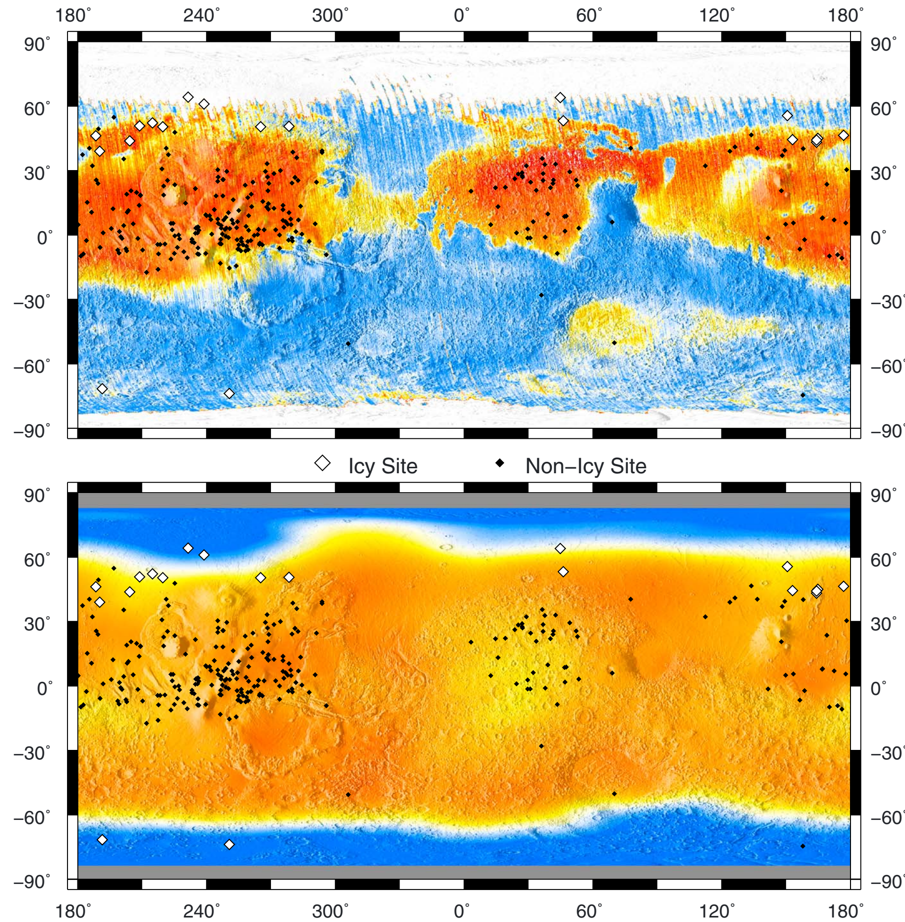

Figure 3. Global distribution of new impacts ([*Daubar et al.*, 2013] and subsequent detections through $L_S = 0°$, MY32). White symbols indicate ice-exposing impacts; black indicates no visible ice. (top) Background is the TES dust cover index map of *Ruff and Christensen* [2002], available at http://www.mars.asu.edu/~ruff/DCI/dci.html;; warm colors indicate dusty areas. New craters are preferentially detected in dusty areas. (bottom) Background is water-equivalent hydrogen from *Feldman et al.* [2008]; cool colors indicate high hydrogen content.

the same effect. Geographic variations in the density of CTX repeat image coverage might also affect the detection of new craters.

In the north, a handful of new impacts have been found at latitudes where ice is expected but show no evidence for visible ice. In some cases, these sites also show geomorphic evidence for ice in the form of thermal contraction polygons. The most likely explanation for this is that the craters did not excavate deeply enough to reach ice, which is expected to be at a depth of at least tens of centimeters around 45°N. An alternate possibility is that ice was exposed and then, before initial images were acquired, sublimated enough to become indistinguishable from regolith. Pore-filling ice in particular is likely to be indistinct, since such ice is relatively dark and became indistinguishable from dry regolith within days at the Phoenix site [*Smith et al.*, 2009b]. Unfortunately, sites nearest the stability boundary are also those where sublimation is likely to be most rapid. It is also possible that ice is discontinuous, but this possibility is not favored since ice should be present due to vapor deposition wherever it is stable [e.g., *Mellon and Jakosky*, 1993]. The fact that clean ice is usually exposed suggests that it is quite widespread.

Figure 4 shows the northern hemisphere crater diameters as a function of latitude, indicating whether or not ice was observed. For cluster sites, the diameters of all the ice-exposing craters are plotted, along with one or more of the largest ice-free craters. The right-hand axis shows 0.084 times the crater diameter, an estimate for the maximum excavated depth. (The excavation depth is approximately one

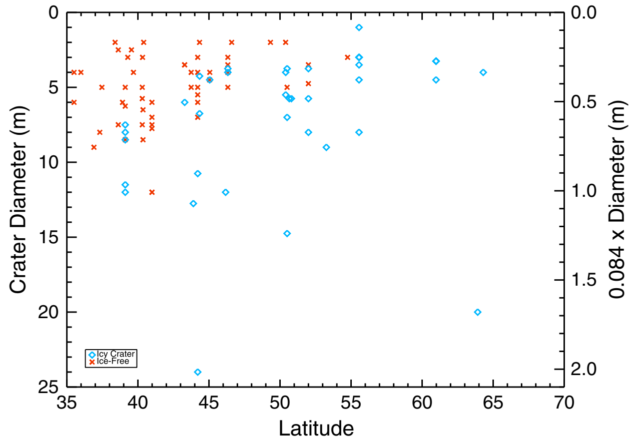

Figure 4. Crater diameters versus latitude for ice-exposing and non-ice-exposing craters. Blue symbols indicate craters with visible ice and red indicate no visible ice. All icy craters are shown; at sites with ice-free craters, one or several of the largest ice-free craters are plotted. The right axis gives an estimate of the maximum excavation depths.

tenth of the transient crater diameter, which is ~0.84 times the final diameter for simple craters [*Melosh*, 1989].) Note that this estimate could be inaccurate due to interactions with the ice table, which provides a significant strength contrast and likely influences the flow of material during crater excavation. This could result in a shallower excavation depth. Several craters with and without ice have flat-floored or terraced morphologies consistent with a strength contrast in the subsurface [*Melosh*, 1989]. Nevertheless, the distribution of ice depth versus latitude implied by Figure 4 resembles model stability profiles for ground ice, with high-latitude shallow ice giving way to deeper ice and a sharp latitudinal cutoff. Some "blurring" of this profile is expected since the thermophysical properties and elevations of the impact sites are not uniform (Table 1) and because some craters without visible ice may expose pore ice.

A few small new craters at lower latitudes have exposures of relatively bright material that we interpret to be light-toned rock or regolith. Some exposures are quite small and confined to the crater cavity, while in other cases, most of the ejecta is relatively bright. In cases where such craters are significantly equatorward of predictions for ground ice, we consider the null hypothesis to be that these exposures are not ice. Monitoring over time has so far revealed only gradual changes consistent with eolian effects, while we would expect sublimation to be particularly rapid at low latitudes. In cases near the equator where most of the ejecta is relatively light-toned material, we can be confident that it is not ice because if it were, it would require that the shallow subsurface be extremely ice rich, and we should also see thermal contraction polygons and sublimation landforms.

3.2. Ice Stability

We examined the stability of ground ice at each of the impact sites using a model based on that of *Mellon et al*. [2004]. The model calculates the vapor density at the ice table for various ice depths using a one-dimensional thermal model. The model solves the heat conduction equation with upper boundary conditions given by insolation and emitted radiation. Atmospheric thermal radiation is modeled by using the Ames 1-D radiative transfer code (available at http://spacescience.arc.nasa.gov/mars-climate-modeling-group/brief.html) to generate a lookup table for downwelling radiation as a function of surface albedo, emissivity, temperature, pressure, incidence angle, solar distance, and atmospheric temperature. Atmospheric temperature was tracked at the top of the convective layer [*Hinson et al*., 2008]. In the lookup table, the lapse rate to the surface was linearly interpolated between the atmospheric and surface temperatures but bounded by 0 and −4.9 K/km (the adiabatic lapse rate). This is a simplistic model, but the detailed temperature structure of the atmosphere is not essential here. Thermophysical properties differ above and below the ice table depth. The annual average vapor pressure is found for each ice table depth, and these values are then interpolated to find the depth where the ice table vapor pressure matches a latitude- and elevation-dependent estimate for the atmospheric average, using the methods of *Mellon et al*. [2004].

The water abundance is an important parameter. The critical boundary condition is the near-surface annual average water vapor content, but in the absence of accurate measurements of this value at the impact sites, we estimate it following *Mellon et al*. [2004]. *Mellon et al*. [2004] found that the best fits to the current ice distribution from GRS data were obtained using 10 or 20 precipitable micrometers annual average water vapor content. These values are for the annual average column abundance at 0 km

Table 3. Nonicy Impact Sites Above 40°N

Latitude[a]	Longitude[a]	Largest Crater Diameter (m)	Atmospheric water (pr μm)[b]	Why Ice Not Observed
40.1	157.93	8	36	Unstable
40.31	221.22	7.25[c]	14	Pore ice?
40.33	185.5	3	31	Unstable
40.36	136.57	8.75[c]	22	Pore ice/marginal stability
40.41	77.61	1.75	67	Unstable
40.99	126.31	12.5[c]	32	Unstable
43.75	203.32	5.25[c]	22	Pore ice/too shallow/marginal stability
46.6	133.7	2.75	17	Too shallow
47.7	225.1	7.75	6	Pore ice?
49.33	189.68	1.75	12	Pore ice or inadequate exposure
54.76	196.85	2.75	4	Pore ice or inadequate exposure

[a]Planetocentric latitude and east longitude.
[b]Minimum atmospheric water content for stable ice at this location.
[c]Flat-floored crater.

elevation, and the estimated near-surface vapor density is scaled as a function of latitude and elevation in the stability calculations, assuming that water vapor is distributed uniformly with atmospheric CO_2. In the discussion below, all references to column abundances refer to this normalized value. For comparison, *Smith* [2002] gives an annual average of around 17 pr μm from 10°S to 40°N and 12 pr μm elsewhere (normalized to a 610 Pa pressure level, roughly equivalent to −1.6 km elevation [*Smith and Zuber*, 1998]) using data from the Thermal Emission Spectrometer (TES) [*Christensen et al*., 2001]. Some disagreement about the annual average between different data sets has been reported, suggesting that the initial TES values may be somewhat high [*Fouchet et al*., 2007; *Fedorova et al*., 2010]. *Wolkenberg et al*. [2011] found better agreement, with a lower annual maximum from TES than *Smith* [2002]. TES annual averages from *Smith* [2008] are also slightly reduced. Interannual differences are also reported [e.g., *Smith et al*., 2009a]. Regardless of these issues, the ice distribution reflects the average value over time scales much longer than those spanned by spacecraft observations.

We iteratively determined the minimum atmospheric water content to stabilize subsurface ice at each site for Mars' current orbit. The results are summarized in Table 1. Not surprisingly, only small amounts of water vapor are required to stabilize ice at higher latitudes. *Byrne et al*. [2009] used results from *Mellon et al*. [2004] for 10 and 20 pr μm of atmospheric water vapor and found that ice was stable at sites 1–5 in the 20 pr μm case but was unstable at the lower latitude sites for 10 pr μm. Our minimum water values approximately agree with this. Site 18, which is the lowest-latitude site, requires a modestly higher atmospheric water content of 25 pr μm.

Table 3 presents results of the same modeling for new impact sites without ice at latitudes above 40°N. Taking 25 pr μm as the best estimate for the long-term average, ice is expected at several of these sites, but in some locations, the craters may be too shallow to reach it. Intriguingly, in multiple cases where the ice is expected and craters are large enough to reach it, the craters are flat floored, consistent with excavating to the top of the ice table but only showing pore ice as discussed above. However, other resistant layers could produce the same morphology.

4. Site Morphologies

4.1. Local Geomorphology

The geomorphic settings of the ice exposures are varied. On a broad scale, they occur in two general settings: on or near lobate aprons associated with hills and mesas and on unremarkable swaths of the northern plains. In general, most of the impact sites with visible ice at latitudes below 50°N are on or near lobate aprons while those at higher latitude are on plains, but this is not an absolute distinction. Sites 9 and 17 occur on the ejecta of much older craters; it is likely that these craters are so much older that the surface has been subjected to considerable modification, so the fact that they are on ejecta rather than typical plains regolith may have little significance. The ice stability boundary has varied widely since the older craters formed. Site 16 occurs in material filling an older crater, possibly related to the midlatitude mantle [*Mustard et al*., 2001]. At all sites,

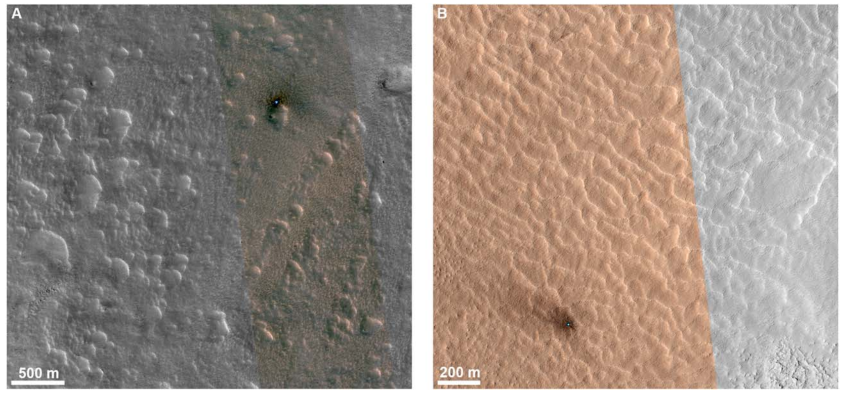

Figure 5. (a) Broad view of site 11, showing that the (upper right) impact occurs in a field of scalloped depressions that open toward the southwest (HiRISE image ESP_017926_2310; north is up, and light is from the left in both panels). (b) Scalloped-ridge texture at site 2 (HiRISE image PSP_010084_2235).

small craters other than the new impacts are rare, indicating a significant level of surface modification over time scales comparable to the formation interval for small craters.

The immediate surroundings of the craters (beyond the ejecta) generally have scattered boulders, often up to meter scale. In this respect, the impact sites are typical of the northern plains, which are commonly rocky [*McEwen et al*., 2007b; *Golombek et al*., 2008]. Boulder rings are observed at several sites; these are interpreted as relics of the rims and ejecta of extremely degraded craters.

The surface of most sites at least hints at a regular, patterned texture. Several have well-developed polygonal surface patterns interpreted as thermal contraction polygons. The most prominent examples are at sites 1 and 5, which include features that fall on a gradation between the "peak-top" and "flat-top small" classifications of *Levy et al*. [2009] (Figures 1a and 1e). Morphologies at other sites include varying degrees of polygon development or rolling, regular hummocks. Several sites do not have well-defined polygons with distinct troughs but do have regular hummocks or ridges. Site 14 occurs on a surface of aeolian ripples. If the ripples are active, this shifting surface might preclude development of organized polygons.

Site 11 occurs in a field of elliptical pits or scalloped depressions. These features (Figure 5a) resemble depressions that occur in Utopia Planitia and south of the Hellas basin [e.g., *Morgenstern et al*., 2007; *Lefort et al*., 2009, 2010] but are not oriented toward the pole. Also, unlike those features, many of the scallops at site 11 have central knobs or pits. Dense-packed ridges or scarps with some resemblance to scallops are also observed around craters at sites 2, 4 and 7, and in poorly developed form at site 8 (Figure 5b). These features are generally oriented toward the west or southwest.

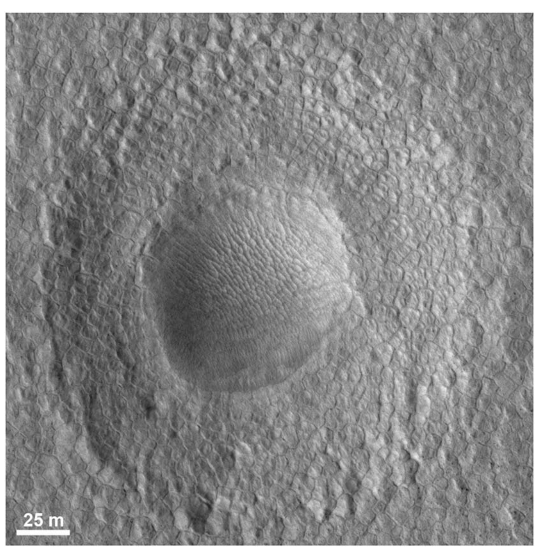

Figure 6. Apparently expanded crater with steeper inner cavity near site 15, possibly due to thermokarst expansion (HiRISE image ESP_025642_2310; north is up, and light is from the left).

At several sites, nearby older craters have shallowly sloped walls leading down to a slightly steeper, bowl-shaped central depression, suggestive of expansion of the craters (Figure 6). These features may have formed via thermokarstic growth of impact craters in ice-rich targets.

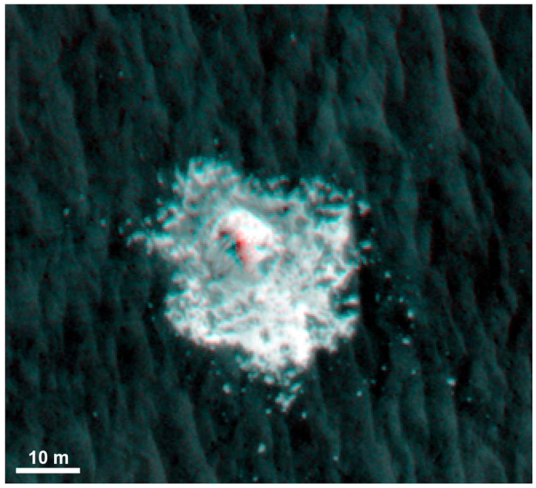

Figure 7. Anaglyph of site 14 (Figure 1o). Note the icy block within crater. (Anaglyph constructed from HiRISE images ESP_025840_2240 and ESP_025906_2240. North is up. Images have been given a nonlinear stretch to make both bright ice and dark background visible.)

One of the two icy craters in the southern hemisphere (site 19) occurs on or near a thin outlier of the SPLD. These deposits are thought to be a mix of atmospherically deposited ice and dust, so an ice exposure is unsurprising. The surface has scattered boulders even at this site.

4.2. Crater and Ice Morphologies

Most of the ice-exposing craters appear to have standard bowl-shaped morphologies (e.g., Figure 7), although interpretation of the topography can be difficult because the ice produces large variations in brightness within the cavity. Ice-free craters at several cluster sites have flat floors (e.g., Figure 8), suggesting that they excavated to the top of a resistant layer [*Melosh*, 1989]. Given the depths and the evidence for ice, this probably represents the top of the ice table.

The distribution of visible ice in and around craters is highly variable. In general, ice is confined to the crater cavity in smaller impacts but reaches over the rim in larger craters and eventually dominates the ejecta. At site 9, small patches of ice occur at many crater radii past the rim (Figure 1i), well beyond the continuous ejecta blanket. Within the craters, ice is ubiquitous but often patchy; the walls and floor are not uniformly covered. In the cases where ice occurs outside the crater, it generally drapes or comprises the crater rim. However, at site 11, a part of the rim has no visible ice despite the presence of exterior ice (Figure 1k).

The azimuthal distribution of ice in ejecta ranges from generally symmetric (e.g., site 9; Figure 1i) to extremely uneven (e.g., sites 2 (Figure 1b) and 5 (Figure 1e), where all visible ice outside the cavity is confined to an approximately 90° sector). There are several cases where ice is concentrated on pole-facing slopes, consistent with slower sublimation and longer preservation on colder surfaces. However, in other cases, it is most prominent on slopes with other orientations, and thus, the asymmetry likely dates from the impact rather than developing later. This could be due to oblique impacts and/or variations in the original ice distribution.

Several of the impact sites are actually clusters of craters, formed when the incoming projectile fragmented in the atmosphere [e.g., *Ivanov et al*., 2009]. In a given cluster, it is usually the case that ice is visible in larger and absent in smaller craters. However, this is not an absolute rule; at site 1, ice is not observed in the largest crater with a diameter of 5 m [*Dundas and Byrne*, 2010, Figure 6] but is seen in two craters with diameter around 4 m

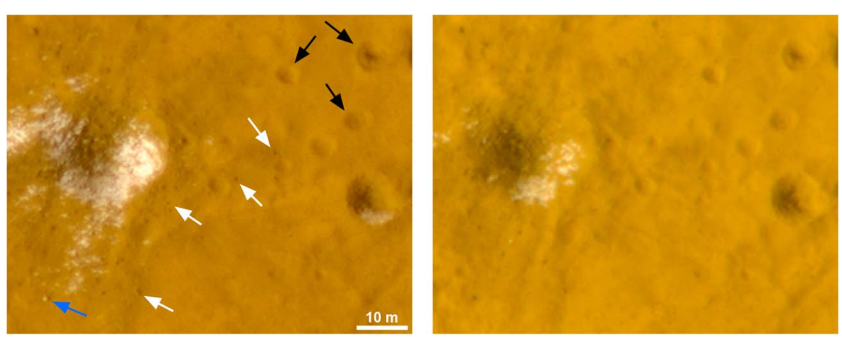

Figure 8. Features of icy site 7 in HiRISE images ESP_016954_2245 and ESP_026092_2245. Black arrows indicate examples of craters with flat or terraced floors suggesting impact into a layered target with a strong underlying layer, likely the ice table. White arrows indicate examples of meter-scale blocks that have shrunk or disappeared in the later image. Blue arrow indicates an icy block of ejecta, which may contain a significant amount of regolith since it is still partially present in the later image. All lighting angles match to within 2°. Changes are consistent in other images at slightly different times. North is up and light is from the left. An animated GIF of this comparison is available in the supporting information.

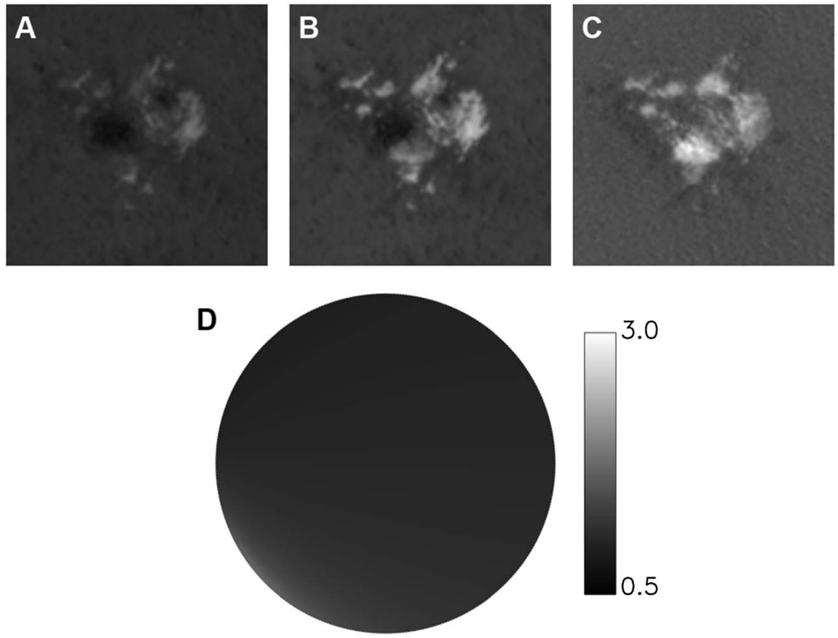

Figure 9. HiRISE red-channel RDR I/F values for (a) ESP_016783_2360 and (b) ESP_017706_2360 on the same scale, after an approximate atmospheric correction was applied. (c) Ratio of corrected I/F values. The background brightness changes slightly due to errors in the atmospheric correction, but this effect is not large enough to account for observed brightening of ice. (d) Model of brightness changes due to the small lighting changes between the two images. The plot is a polar plot with coordinates of slope (0–40°, the radial coordinate) and slope orientation, arranged to approximately simulate looking down into a crater (i.e., the top of the circle represents a south facing slope). The brightness of the polar plot is given by the ratio of the cosines of the incidence angles for those slopes and aspects and the lighting conditions of the two images. The brightness ratio scale bar applies to both Figures 9c and 9d. Essentially none of the variation seen in Figure 9c can reasonably be attributed to different lighting.

(Figure 1a), where the excavation depth is ~10 cm shallower. At site 11 (Figure 1k), no ice is visible in a 5 m crater, but ice appears on the floor of a 3.75 m crater. However, the smaller crater overlaps the rim of a larger crater in the cluster, which might have ejected ice.

Secondary craters are also observed, most notably at sites 7 and 19. These can be distinguished from cluster primaries by the radial nature of dark blast striations. It is noteworthy that such small craters can produce substantial secondary fields, although not in all cases. The presence of a strong cementing ice layer may have some effect on secondary production for these craters.

5. Changes Over Time

5.1. Changes to Ice

The ice patches at each crater both fade and shrink over time, eventually reaching a color and brightness similar to the surrounding regolith, which is often darker than the original surface due to removal of dust. Since the dark blast zone can outlast the ice, the disappearance of the ice is not due only to burial by air fall dust. The general pattern is for ice to disappear from small craters and distal ejecta first and persist longest in the cavity or proximal ejecta of the largest craters.

In a few cases, icy surfaces apparently became brighter. In order to determine whether the apparent brightening was due to real surface changes, we examined an example at site 3 in more detail (Figure 9). We compared two images (ESP_016783_2360 and ESP_017706_2360) with very similar lighting and roll angles, such that small areas could be registered at the pixel level. We performed an approximate atmospheric correction by subtracting the I/F (intensity/flux) of the darkest shadow pixel, on the assumption that all of the brightness of that pixel was due to scattered atmospheric light. This correction is not precise but should roughly normalize the atmospheric effects in each image. The shadow correction was approximately equal in both images, which is expected since the images were acquired close together in time and are likely to have

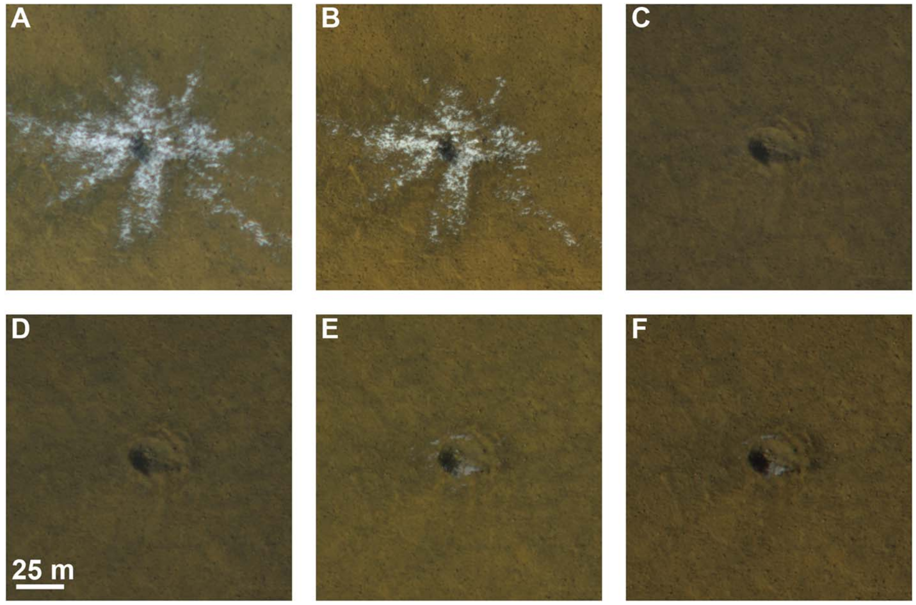

Figure 10. Changes at site 9 over time. Over the initial summer after impact, the ice (a) fades and (b) shrinks somewhat. It is then essentially invisible at the start of the following (c and d) spring before (e) rebrightening and (f) fading again. All images have been given an approximate correction for atmospheric haze by subtracting the I/F value of the darkest pixel in the scene and then given identical stretches over the same range of corrected I/F. This atmospheric correction is imperfect, which may account for some of the variation in the appearance of the ground around the crater. The rest is likely due to different lighting angles. (Figures 10a–10f: HiRISE images ESP_017868_2440, ESP_018646_2440, ESP_024949_2440, ESP_025516_2440, ESP_026505_2440, and ESP_027982_2440. North is up, and light is from the left in all images.)

had similar atmospheric conditions. We then took the ratio of these corrected I/F values. This corrected ratio is shown in Figure 9c and compared with the ratio expected due to the known lighting differences. The observed changes are much greater than can be explained by the slight difference in lighting.

The timing of fading and shrinking can be complex; image series unambiguously demonstrate progressive fading and shrinking of ice patches during the summer, but in several cases, there are dramatic changes between the last summer image and the first of the following spring (e.g., Figure 10). This is particularly common at latitudes above ~50°N. Such changes could be due in part to late summer sublimation, but it is also likely that in some cases, the ice is buried by thin layers of dust over the course of the winter, perhaps incorporated into the seasonal CO_2 cap (see section 5.2). Figure 11 summarizes the time scales for ice persistence in the largest crater at each site, based on interpretation of HiRISE observations. Images were stretched for contrast and material that was relatively bright in the HiRISE BG band ("white" or "blue" in enhanced color) was interpreted as ice. A significant fraction of images were interpreted as ambiguous, due to shadowing or the fact that we are observing small patches of ice that disappear in a gradational manner.

A particularly interesting change occurred at site 7, where blocks of ejecta material shrank or disappeared during the monitoring period (Figure 8 and Animation S1 of the supporting information). These blocks range up to meter scale. In all but one case, they were not visibly icy based on HiRISE color data, which may indicate that they developed an opaque sublimation lag between the impact and acquisition of the first HiRISE image, but the blocks are barely resolved and the BG and IR channels in the initial image were acquired at lower resolution, 60.8 cm/pixel. Sublimation rates on exposed blocks are likely to be significantly higher than on level surfaces, particularly on the Sun-facing sides, so a lag could develop more quickly. The blocks protrude into the wind and rest on top of insulating regolith, which would also speed sublimation.

5.2. Changes to Dark Blast Zones

There is a distinct latitudinal dependence to the behavior of dark blast zones. Below ~50°N, they may slowly fade over time but can remain quite distinct for at least several Mars years. Above ~50°N, the dark blast zones typically disappear entirely or even become brighter than the surroundings within the first winter after the impact. The most likely explanation for this is that they are reworked by the seasonal polar cap, a mixture of

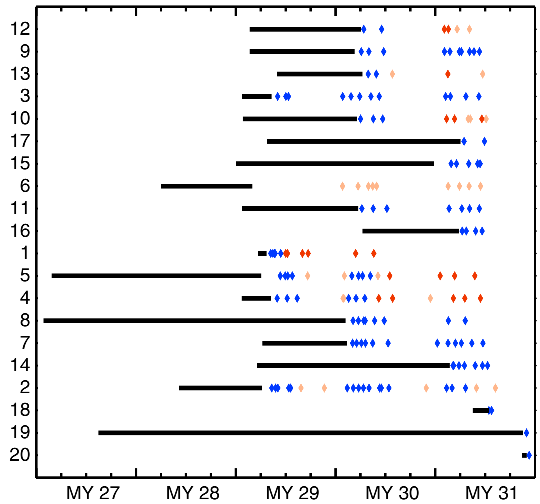

Figure 11. Timing of images and persistence of ice. Blue diamonds indicate images with definite visible ice, tan indicates uncertain images (ranging from "probable" to "unlikely" ice), and red indicates images with no visible ice. Uncertainty in interpretation may be due to shadows, difficulty separating topographic and albedo effects, or simply the ambiguity inherent in interpreting the end point of a gradational process. Black bars indicate discovery intervals. Left axis gives site number, ordered by latitude. In some cases, ice patches have remained visible (although faded and shrunk) for more than two Mars years. No HiRISE image of site 6 shows unambiguous ice, but we are confident that this impact exposed ice based on the CTX discovery image (Figure 2). The crater cavity does appear to have some relatively bright material, but it is difficult to distinguish from topographic effects. The first HiRISE image was not acquired until after a Mars winter had passed.

dust, water frost, and (mostly) CO_2 ice. The continuous seasonal CO_2 cap extends to approximately 50°N, although H_2O frost reaches near 45°N [e.g., *Appéré et al*., 2011], so this reworking may be as simple as burial by the dust component of the cap. Additionally, sublimation at the base of the cap reworks the surface at high latitudes [e.g., *Kieffer*, 2007] and could have lesser effects as long as the CO_2 ice is thick enough to allow pressure to build up. Simple loading by the cap could also modify surface textures.

6. Discussion

6.1. Atmospheric Water Content

We found that atmospheric water contents as high as 25 pr μm (column abundance at 0 km elevation) are needed for ice stability at the lowest-latitude (least stable) sites. Given various sources of uncertainty, we caution against overemphasizing specific values. The primary result of the modeling is that the distribution of ice in the northern hemisphere is broadly consistent with an atmospheric water content of at least twice the present value, assuming that H_2O is well mixed with CO_2. The relevant value of near-surface water vapor density represents the long-term average, where "long term" is the time scale for ice to adjust to new climate conditions. (This definition is inherently loose since sublimation and deposition rates vary with temperature, burial depth, and atmospheric water content, but substantially filling the pore space of initially dry regolith may require tens of thousands of years [*Mellon and Jakosky*, 1993], while centimeter-scale adjustments of the ice depth take ~100–1000 years [*Mellon et al*., 2004].) A higher average water content is consistent with the results of *Chamberlain and Boynton* [2007], who suggested that it could vary by a factor of ~3 in the recent past due to variation in the longitude of perihelion (with ~50,000 year period) and is presently near a minimum.

Alternatively (or additionally), the near-surface humidity could be higher than expected based on column abundances if the water vapor is concentrated near the surface rather than well mixed. This is consistent with the interpretations of humidity measurements made by the Phoenix Lander [*Zent et al*., 2010] and with some low-resolution atmospheric profiles [*Smith et al*., 2011]. This possibility could affect the stability of apparent near-surface liquid flows attributed to brines [*McEwen et al*., 2011]. A third possible effect is that stable ice could be more extensive than expected if the vapor pressure above the ice table is controlled by brines formed by deliquescent salts in the regolith. Salty solutions have a reduced vapor pressure, and deliquescence might maintain a lower vapor pressure, thereby reducing the rate of diffusion to the atmosphere. *Mellon et al*. [2009] considered this unlikely since at that time salts at the Phoenix landing site were thought to be uniformly distributed in the soil [*Hecht et al*., 2009], while liquid would concentrate salts as it evaporated. However, subsequent work has suggested concentrations of deliquescent perchlorate salts, consistent with occasional small-scale melting [*Cull et al*., 2010a]. Either of these effects would make ice more stable and widespread under all climate conditions.

6.2. Nature of Visible Ice

The nature of Martian ground ice is an important question. A common assumption is that ground ice fills the pore spaces of regolith (pore ice), which is a natural consequence of atmospheric vapor deposition [*Mellon and Jakosky*, 1993; *Hudson et al*., 2009]. However, recent observations have demonstrated the occurrence of ice contents greater than the natural soil pore space (excess ice). The frequency, distribution, and thickness of excess ice are important in understanding the full range of permafrost processes on Mars because such ice probably did not form via simple vapor deposition.

Observations of excess ice on Mars include direct excavation of ice with less than 1% soil content by the Phoenix Lander [*Smith et al*., 2009b; *Mellon et al*., 2009; *Cull et al*., 2010b]. On a regional scale, near-surface volumetric ice contents up to 85% have been suggested to extend over broad areas at high latitude based on GRS data, which probe depths of a meter or less [e.g., *Boynton et al*., 2002; *Prettyman et al*., 2004; *Feldman et al*., 2008, 2011]. Volume fractions of 50–100% ice have been suggested to extend to a few tens of meters depth in the northern hemisphere based on radar observations [*Mouginot et al*., 2010]. The high end of this range would indicate large amounts of very clean excess ice. *Levy et al*. [2008; 2009] suggested that some thermal contraction polygon morphologies indicate excess ice, although *Mellon et al*. [2008b, 2009] argued that such ice is not volumetrically dominant in the upper 3–5 m and has little effect on polygon morphology, based on modeling of polygon dimensions.

A number of processes have been proposed as the source of excess ice on Mars, including vapor diffusion coupled with thermal expansion and contraction to create extra pore space [*Fisher*, 2005] or burial of snow deposited under past climate conditions driven by orbital variations [e.g., *Head et al*., 2003; *Mischna et al*., 2003; *Levrard et al*., 2004; *Schorghofer*, 2007; *Schorghofer and Forget*, 2012]. *Mellon et al*. [2009] favored ice lens formation through migration of thin films of liquid present at subfreezing temperatures at the Phoenix landing site; work of *Sizemore et al*. [2013] using the model of *Rempel* [2007] suggests that this is plausible. Frozen floodwaters, pingos, or buried glaciers have been considered but are unlikely to be the sources of regionally extensive excess ice [*Mellon et al*., 2008a]. Debris-covered glaciers have been observed in some locations in radar data [*Holt et al*., 2008; *Plaut et al*., 2009]. The lobate aprons where some craters expose ice may be such features, but they are not ubiquitous across the northern plains.

Byrne et al. [2009] and *Dundas and Byrne* [2010] suggested that the impact-exposed ice also represents excess ice, at lower latitudes than indicated by GRS data, and thus, that excess ice is widespread. Here we further discuss this issue. The ice visible at the crater sites described here is clean ice with low regolith content, based on sublimation modeling [*Dundas and Byrne*, 2010]. The observed persistence time scales indicate that the ice remains visible through a period in which one or more millimeters of exposed ice should sublimate. This conclusion is reinforced by the continued visibility of ice well beyond the intervals considered by *Dundas and Byrne* [2010], and the observed brightening at several sites suggests that lags are occasionally stripped away, most likely by wind. Direct deposition of new frost on level surfaces (as seen in Figure 9) is unlikely since the high thermal inertia of ice means that near-surface ice is warmer than the surroundings during the coldest part of the night, but it is possible that condensed particles could settle out. Modeling by *Kossacki et al*. [2011] also indicates millimeters of sublimation during the period in which ice remained visible. *Kossacki et al*. [2011] proposed that darkening was due to changes in optical properties rather than lag development, but even in this scenario, the persistence of visible ice requires that it be clean, or an opaque lag would be produced before other changes became relevant. The observed brightening is also more consistent with lag development and removal since vapor-deposited frost would be very clean.

Excavated excess ice in the craters is also consistent with the observations by the Phoenix Lander. Exposed pore ice there was darker than ice-free soil [*Mellon et al*., 2009] and receded beneath an opaque lag within a few days, whereas excess ice remained visibly bright for months while sublimating several millimeters [*Smith et al*., 2009b]. Icy crater ejecta should sublimate particularly quickly, since an insulating layer of regolith below will raise peak temperatures in the thin icy ejecta layer. This is consistent with the general tendency for the crater cavities to remain icy longest.

However, it is possible that the impact process has affected the observed ice. Modeling of the impacts at sites 1–5 by *Reufer et al*. [2010] indicates that some amount of melting is likely in the larger craters, although none is expected in the smaller craters with relatively deep ice. (Note that this is likely even if ice has a higher effective strength than that used by *Reufer et al*. [2010] in estimating crater sizes, because the smaller craters mostly excavate regolith, making this parameter less important.) We have not observed any flow-like morphologies that might suggest that ejecta was fluid mud but cannot rule out smaller amounts of melting. The most important question is whether clean surface ice forms from pore ice, since this could make it difficult to distinguish preexisting excess ice. Melting by an impact into pore ice would initially produce mud. This could produce clean ice if water seeped from wet mud, pooled, and froze before reinfiltrating. This process depends on a number of factors, including the local regolith permeability and grain size (smaller grains will have a larger contact area for heat exchange with infiltrating water), the regolith salt content leading to brine formation, the temperature of regolith material in the ejecta and crater cavity, the size and shape of depressions in which water could pool, the temperature reached by the meltwater, and even the season and time of day of the impact. This system is difficult to model, as it is complex and poorly constrained. An additional complication is that recondensation of water vapor frost might occur at the rapidly cooling surface, but the very heterogeneous covering of many crater cavities and ejecta (Figure 1) suggests that this is not the dominant process.

It is also possible that the high temperature of ejecta and crater bowl material could drive the desiccation of the topmost layer of mud. The Lunar Crater Observation and Sensing Satellite impact experiment used a projectile with kinetic energy comparable to some cases modeled by *Reufer et al*. [2010] and produced a crater that *Schultz et al*. [2010] estimated was 25–30 m in diameter. *Hayne et al*. [2010] estimated that parts of the crater were heated to over 950 K, which would drive extremely rapid loss of water or ice.

Regardless of the events in the complex Martian environment immediately after impact, several observations indicate that much of the observed ice was originally clean—that is, excess ice. Some blocks of ejecta at site 7 were visibly icy in early HiRISE images (Figure 8 and Animation S1 of the supporting information), and it is unlikely that significant pooling or condensation would be concentrated on ejecta blocks. Icy, blocky material has also been observed elsewhere (Figure 7). The disappearance of half-meter-scale blocks at site 7 (Figure 8) also strongly suggests that they were mostly composed of excess ice. Alternatively, it is possible that the blocks of ice-cemented regolith could disappear if high winds occurred after sublimation caused the blocks to disaggregate. After a dust storm at the Viking Lander 1 site, centimeter-scale changes were observed in materials that had previously been disturbed by the lander, and peak winds need only have lasted for seconds [*Moore*, 1985]. However, the dark blast zone remained prominent at site 7 after block disappearance, suggesting that aeolian effects have not been great over the same time period.

Visible ice occurs in small craters where the regolith cover was likely decimeters thick; based on the modeling of *Reufer et al*. [2010], it is unlikely that significant melting occurred there. There are also a number of small craters with no visible ice even though nearby craters of comparable size do have such ice (Figure 4), and in several cases, they have flat or terraced floors (Figure 8) indicating interaction with a strong layer, probably the ice table. Burial by the ejecta of other craters could occur in some cases. However, at site 1, the largest crater has no visible ice and sits in a part of the cluster with few nearby craters, while the icy craters were downrange and in a more dense part of the cluster, suggesting that burial is not the reason that ice is not seen in the largest crater. These observations indicate that such craters do not produce much clean ice in the impact process, and thus, where it is observed in similarly sized craters, it is likely to predate the impact.

Therefore, while some of the observed clean ice may have been produced by impact, in other cases, it is likely to be original excess ice with low regolith content. Spectral modeling of the craters by *Cull et al*. [2012] suggested regolith contents on the order of 1%, similar to that observed by the Phoenix Lander. Although the origin of the clean ice is uncertain in some cases, these craters suggest that excess ice is common where ground ice is found, at least in the relatively high-albedo regions where we can detect new impacts. However, the differences between comparably sized craters within individual clusters also indicate that there are heterogeneities in ice content on short-length scales. Variable distributions of ice around craters may also be due to heterogeneities in the ground ice, if they are not caused by oblique impacts.

Models for the origin of excess ice must account for this heterogeneity, as well as the common presence of boulders on the surface. Both of these observations are problematic if the ice is the result of a snowpack from a very recent "ice age," since there has been little time for impacts to garden boulders to the surface or for local heterogeneities to develop. However, the presence of boulders on the SPLD outlier at site 19 demonstrates that such gardening can occur at some level. (The estimated surface age of the SPLD is 30–100 Ma [*Koutnik et al*., 2002], but gardening may be faster on thinner ice.) An older snowpack could avoid these issues but must survive in midlatitude regions with episodic instability. One model by *Schorghofer and Forget* [2012] suggests that an ice sheet formed 863 ka ago could persist to the present at the latitude of the icy craters, while one from 4.45 Ma would not. However, the younger ice sheet would allow less time for impact gardening. Complete gardening to a depth of even 1 m requires hundreds of millions of years [*Hartmann et al*., 2001] but the time scale to distribute boulders over the surface could be less. It remains to be seen whether the other parts of parameter space can make this model entirely consistent. The enhanced vapor diffusion model of *Fisher* [2005] is consistent with surface boulders but required several Ma to produce high ice contents below depths of a few decimeters and did not consider the variations in temperature, water vapor abundance, and ice stability that have occurred over that time frame. Ice lenses could form within soil containing boulders and be heterogeneous if the regolith is nonuniform. However, *Sizemore et al*. [2013] suggest that ice lensing should produce lenses between 5 and 20 cm depth. Most of the craters excavate to these depths, yet we observe that larger craters appear icier and do not see clear evidence for confinement of ice to such a layer—ice is observed throughout the walls of the large craters at sites 7 (Figure 1g) and 9 (Figure 1i), which excavated to >2 m depth. This interpretation is complicated by potential slumping of ice on the walls and the possibility that some of the clean ice was produced during the impact event. In some cases, the ice may be the core of lobate aprons like those observed by radar [*Holt et al*., 2008; *Plaut et al*., 2009]. This suggests that the covering lag is thin (*Holt et al*. [2008] could only constrain it to be less than 10 m). At site 19, it is likely that the exposure is SPLD ice, presumably deposited from the atmosphere. Visible ice at site 19 is consistent with a very low dust content for the near-surface SPLD and a very thin dust lag. However, both on the SPLD and on ice-rich lobate aprons, other ice formation processes within lag deposits cannot be ruled out.

The lack of bright, clean ice in the two previously known new craters in the southern mid-latitudes was consistent with the hemispheric asymmetry in volumetric ice content suggested by *Mouginot et al*. [2010]. However, the quality of the HiRISE data for one of these sites is poor. At the other site, the initial image had a high incidence angle, which can make ice hard to distinguish, and the seasonal cap could have modified the surface before the second image was acquired. Three southern hemisphere craters have since been discovered at mid-latitudes to high latitudes. One of the newly found craters impacted the SPLD and another impacted a possible thin SPLD outlier based on MOLA topography. It is surprising that one of these showed no visible ice, since studies of the SPLD suggest bulk dust contents of 0–10% [*Plaut et al*., 2007] or 15% [*Zuber et al*., 2007]. The ice-free crater may not have been large enough to penetrate a dust lag. Alternatively, a bulk ice content of ~10% is consistent with small-scale variations between very clean and dust-rich layers, and the crater could have formed in the latter. The third new southern impact site is off the SPLD and does show bright material. This suggests that clean ice exists in the south as well, but the present data set is not large enough to draw strong conclusions. We note that GRS data do suggest high volumetric ice contents in the south [e.g., *Boynton et al*., 2002; *Prettyman et al*., 2004; *Feldman et al*., 2008].

6.3. Periglacial Geomorphology

Thermal contraction polygons are expected to be a good indicator of ground ice on Mars [e.g., *Mellon*, 1997]. We find hints of patterning at most ice-exposing impact sites, although it is often not well developed. Several different polygon morphologies are observed. High-centered polygons at several sites could be consistent with the sublimation-polygon model of *Levy et al*. [2010]. More puzzling is the absence of well-developed thermal contraction polygons immediately around craters at sites 10 and 11 (Figures 1j and 1k), although both have regular rolling hummocks, and polygon troughs occur nearby. One possible explanation for this is that the ice is buried too deeply to experience the strong temperature oscillations required to cause cracking. *Mellon et al*. [2008b] found that for the Phoenix landing site, an ice table depth >20 cm would inhibit polygon formation. This effect should be generally applicable, although the particular limiting depth may vary with latitude and thermophysical properties. However, both impact sites are located in regions where models indicate that ice should occur at very shallow depths, suggesting that small polygons should also occur. It is possible that polygons have not had sufficient time to develop, or they are obscured by a competition with other processes such as eolian resurfacing. Alternatively, they may be too small or have too little relief to be readily distinguished in HiRISE images. Either explanation indicates that the absence of visible, well-defined polygons does not always imply the absence of shallow ground ice. Moreover, if excess ice is common at these sites as discussed above, then there is not a simple relationship between polygon morphology and the occurrence of excess ice.

Scalloped textures and elongate depressions observed at several crater sites resemble features seen in Utopia and south of Hellas. Pole-oriented scalloped depressions in various regions of Mars have been interpreted as thermokarst [e.g., *Morgenstern et al*., 2007; *Lefort et al*., 2009], which forms when excess ice becomes unstable and ice loss drives surface subsidence. Formation of pole-oriented scallops by sublimation of excess ice has been successfully modeled [*Dundas et al*., 2011]. However, the depressions seen in the vicinity of impact sites are often not oriented toward the pole. It is not clear whether this requires a different formation mechanism or simply implies that some regional factor such as wind or long-baseline slopes can influence the orientation. The apparently expanded craters at several sites (Figure 6) may be thermokarst-modified craters. Since thermokarst collapse requires significant quantities of excess ice, visible ice is expected around new craters near thermokarst features. This is indeed observed, supporting thermokarst interpretations of these landforms.

7. Conclusions

New impact craters in the middle to high latitudes on Mars usually expose bright ice. Visible ice occurs at all longitudes where new craters have been discovered, and no regional variations are apparent within the relatively high-albedo regions where new craters can be detected. As predicted by stability models, ice suddenly appears in the mid-latitudes and is seen in the shallowest craters at high latitudes, although the ice may be somewhat out of equilibrium with the climate conditions observed during the period of spacecraft observations. The distribution appears consistent with a long-term average atmospheric water content that is moderately higher than the present value. Alternatively, salts in the regolith could reduce the vapor pressure above the ice table, and/or the near-surface humidity could be higher than expected under the assumption that the water column is well-mixed with the atmosphere.

The ice remains visible for time scales of months to years, indicating low lithic content. Although some clean ice may be produced by the impact, in other cases, it is likely to indicate preexisting excess ice. This suggests that excess ice on Mars is widespread, occurring in most (or all) regions where ice is present in the northern hemisphere, but there may be significant local heterogeneities in its distribution. The common occurrence of boulders on the surface suggests that if the ice began as a snowpack, it is older than expected. An origin by migration of thin films of water is the best explanation for many observations, but snowpack or debris-covered glaciers may be the source in some cases.

Acknowledgments
We thank the HiRISE and CTX operation teams for their work in acquiring and processing the images used in this study. W. Feldman kindly provided the WEH data used in Figure 3. Two anonymous reviewers provided many helpful comments. This work was funded by the Mars Reconnaissance Orbiter Project.

References

Appéré, T., B. Schmitt, Y. Langevin, S. Douté, A. Pommerol, F. Forget, A. Spiga, B. Gondet, and J.-P. Bibring (2011), Winter and spring evolution of northern seasonal deposits on Mars from OMEGA on Mars Express, *J. Geophys. Res.*, *116*, E05001, doi:10.1029/2010JE003762.

Boynton, W. V., et al. (2002), Distribution of hydrogen in the near surface of Mars: Evidence for subsurface ice deposits, *Science*, *297*, 81–85.

Byrne, S., et al. (2009), Distribution of mid-latitude ground ice on Mars from new impact craters, *Science*, *325*, 1674–1676.

Chamberlain, M. A., and W. V. Boynton (2007), Response of Martian ground ice to orbit-induced climate change, *J. Geophys. Res.*, *112*, E06009, doi:10.1029/2006JE002801.

Christensen, P. R., et al. (2001), Mars Global Surveyor Thermal Emission Spectrometer experiment: Investigation description and surface science results, *J. Geophys. Res.*, *106*(E10), 23,823–23,871.

Christensen, P. R., et al. (2004), The Thermal Emission Imaging System (THEMIS) for the Mars 2001 Odyssey mission, *Space Sci. Rev.*, *110*, 85–130.

Clancy, R. T., B. J. Sandor, M. J. Wolff, P. R. Christensen, M. D. Smith, J. C. Pearl, B. J. Conrath, and R. J. Wilson (2000), An intercomparison of ground-based millimeter, MGS TES, and Viking atmospheric temperature measurements: Seasonal and interannual variability of temperatures and dust loading in the global Mars atmosphere, *J. Geophys. Res.*, *105*, 9553–9571.

Cull, S., R. E. Arvidson, J. G. Catalano, D. W. Ming, R. V. Morris, M. T. Mellon, and M. Lemmon (2010a), Concentrated perchlorate at the Mars Phoenix landing site: Evidence for thin film liquid water on Mars, *Geophys. Res. Lett.*, *37*, L22203, doi:10.1029/2010GL045269.

Cull, S., R. E. Arvidson, M. T. Mellon, P. Skemer, A. Shaw, and R. V. Morris (2010b), Compositions of subsurface ices at the Mars Phoenix landing site, *Geophys. Res. Lett.*, *37*, L24203, doi:10.1029/2010GL045372.

Cull, S., C. Dundas, M. T. Mellon, and S. Byrne (2012), CRISM observations of fresh icy craters in mid- to high-latitudes on Mars, Lunar Planet. Sci. Conf. 43, abstract #2145.

Daubar, I. J., A. S. McEwen, S. Byrne, and M. Kennedy (2013), The current Martian cratering rate, *Icarus*, *225*, 506–516.

Dundas, C. M., and S. Byrne (2010), Modeling sublimation of ice exposed by new impacts in the Martian mid-latitudes, *Icarus*, *206*, 716–728.

Dundas, C. M., S. Byrne, and A. S. McEwen (2011), Modeling development of Martian sublimation thermokarst landforms, LPSC 42, abstract 2527.

Fedorova, A. A., S. Trokhimovsky, O. Korablev, and F. Montmessin (2010), Viking observations of water vapor on Mars: Revision form up-to-date spectroscopy and atmospheric models, *Icarus*, *208*, 156–164.

Feldman, W. C., M. T. Mellon, O. Gasnault, S. Maurice, and T. H. Prettyman (2008), Volatiles on Mars: Scientific results from the Mars Odyssey Neutron Spectrometer, in *The Martian Surface: Composition, Mineralogy, and Physical Properties*, edited by J. F. Bell, pp. 125–148, Cambridge Univ. Press, New York.

Feldman, W. C., A. Pathare, S. Maurice, T. H. Prettyman, D. J. Lawrence, R. E. Milliken, and B. J. Travis (2011), Mars Odyssey neutron data: 2. Search for buried excess water ice deposits at nonpolar latitudes on Mars, *J. Geophys. Res.*, *116*, E11009, doi:10.1029/2011JE003806.

Fisher, D. A. (2005), A process to make massive ice in the Martian regolith using long-term diffusion and thermal cracking, *Icarus*, *179*, 387–397.

Fouchet, T., et al. (2007), Martian water vapor: Mars Express PFS/LW observations, *Icarus*, *190*, 32–49.

Golombek, M. P., et al. (2008), Size-frequency distribution of rocks on the northern plains of Mars with special reference to Phoenix landing surfaces, *J. Geophys. Res.*, *113*, E00A09, doi:10.1029/2007JE003065.

Hartmann, W. K., J. Anguita, M. A. de la Casa, D. C. Berman, and E. V. Ryan (2001), Martian cratering 7: The role of impact gardening, *Icarus*, *149*, 37–53.

Hayne, P. O., B. T. Greenhagen, M. C. Foote, M. A. Siegler, A. R. Vasavada, and D. A. Paige (2010), Diviner Lunar Radiometer observations of the LCROSS impact, *Science*, *330*, 477–479.

Head, J. W., J. F. Mustard, M. A. Kreslavsky, R. E. Milliken, and D. R. Marchant (2003), Recent ice ages on Mars, *Nature*, *426*, 797–802.

Hecht, M. H., et al. (2009), Detection of perchlorate and the soluble chemistry of Martian soil at the Phoenix Lander site, *Science*, *325*, 64–67.

Hinson, D. P., M. Pätzold, S. Tellmann, B. Häusler, and G. L. Tyler (2008), The depth of the convective boundary layer on Mars, *Icarus*, *198*, 57–66.

Holt, J. W., et al. (2008), Radar sounding evidence for buried glaciers in the southern mid-latitudes of Mars, *Science*, *322*, 1235–1238.

Hudson, T. L., O. Aharonson, and N. Schorghofer (2009), Laboratory experiments and models of diffusive emplacement of ground ice on Mars, *J. Geophys. Res.*, *114*, E01002, doi:10.1029/2008JE003149.

Ivanov, B. A., H. J. Melosh, and A. S. McEwen (2009), Small impact crater clusters in high resolution HiRISE images—II, Lunar Planet. Sci. Conf. 40, abstract #1410.

Kieffer, H. H. (2007), Cold jets in the Martian polar caps, *J. Geophys. Res.*, *112*, E08005, doi:10.1029/2006JE002816.

Kossacki, K. J., G. Portyankina, and N. Thomas (2011), The evolution of exposed ice in a fresh mid-latitude crater on Mars, *Icarus*, *211*, 195–206.

Koutnik, M., S. Byrne, and B. Murray (2002), South Polar Layered Deposits of Mars: The cratering record, *J. Geophys. Res.*, *107*(E11), 5100, doi:10.1029/2001JE001805.

Lefort, A., P. S. Russell, N. Thomas, A. S. McEwen, C. M. Dundas, and R. L. Kirk (2009), Observations of periglacial landforms in Utopia Planitia with the High Resolution Imaging Science Experiment (HiRISE), *J. Geophys. Res.*, *114*, E04005, doi:10.1029/2008JE003264.

Lefort, A., P. S. Russell, and N. Thomas (2010), Scalloped terrains in the Peneus and Amphitrites Paterae region of Mars as observed by HiRISE, *Icarus*, *205*, 259–268.

Leighton, R. B., and B. C. Murray (1966), Behavior of carbon dioxide and other volatiles on Mars, *Science*, *153*, 136–144.

Levrard, B., F. Forget, F. Montmessin, and J. Laskar (2004), Recent ice-rich deposits formed at high latitudes on Mars by sublimation of unstable equatorial ice during low obliquity, *Nature*, *431*, 1072–1075.

Levy, J. S., J. W. Head, D. R. Marchant, and D. E. Kowalewski (2008), Identification of sublimation-type thermal contraction crack polygons at the proposed NASA Phoenix landing site: Implications for substrate properties and climate-driven morphological evolution, *Geophys. Res. Lett.*, *35*, L04202, doi:10.1029/2007GL032813.

Levy, J. S., J. Head, and D. Marchant (2009), Thermal contraction crack polygons on Mars: Classification, distribution, and climate implications from HiRISE observations, *J. Geophys. Res.*, *114*, E01007, doi:10.1029/2008JE003273.

Levy, J. S., D. R. Marchant, and J. W. Head (2010), Thermal contraction crack polygons on Mars: A synthesis from HiRISE Phoenix, and terrestrial analog studies, *Icarus*, *206*, 229–252.

Malin, M. C., K. S. Edgett, L. V. Posiolova, S. M. McColley, and E. Z. Noe Dobrea (2006), Present-day impact cratering rate and contemporary gully activity on Mars, *Science*, *314*, 1573–1577.

Malin, M. C., et al. (2007), Context Camera investigation on board the Mars Reconnaissance Orbiter, *J. Geophys. Res.*, *112*, E05S04, doi:10.1029/2006JE002808.

McEwen, A. S., et al. (2007a), Mars Reconnaissance Orbiter's High Resolution Imaging Science Experiment (HiRISE), *J. Geophys. Res.*, *112*, E05S02, doi:10.1029/2005JE002605.

McEwen, A. S., et al. (2007b), A closer look at water-related geologic activity on Mars, *Science*, *317*, 1706–1709.

McEwen, A. S., L. Ojha, C. M. Dundas, S. S. Mattson, S. Byrne, J. J. Wray, S. C. Cull, S. L. Murchie, N. Thomas, and V. C. Gulick (2011), Seasonal flows on warm Martian slopes, *Science*, *333*, 740–743.

Mellon, M. T. (1997), Small-scale polygonal features on Mars: Seasonal thermal contraction cracks in permafrost, *J. Geophys. Res.*, *102*, 25,617–25,628.

Mellon, M. T., and B. M. Jakosky (1993), Geographic variations in the thermal and diffusive stability of ground ice on Mars, *J. Geophys. Res.*, *98*, 3345–3364.

Mellon, M. T., and B. M. Jakosky (1995), The distribution and behavior of Martian ground ice during past and present epochs, *J. Geophys. Res.*, *100*, 11,781–11,799.

Mellon, M. T., W. C. Feldman, and T. H. Prettyman (2004), The presence and stability of ground ice in the southern hemisphere of Mars, *Icarus*, *169*, 324–340.

Mellon, M. T., W. V. Boynton, W. C. Feldman, R. E. Arvidson, T. N. Titus, J. L. Bandfield, N. E. Putzig, and H. G. Sizemore (2008a), A prelanding assessment of the ice table depth and ground ice characteristics in Martian permafrost at the Phoenix landing site, *J. Geophys. Res.*, *113*, E00A25, doi:10.1029/2007JE003067.

Mellon, M. T., R. E. Arvidson, J. J. Marlow, R. J. Phillips, and E. Asphaug (2008b), Periglacial landforms at the Phoenix landing site and the northern plains of Mars, *J. Geophys. Res.*, *113*, E00A23, doi:10.1029/2007JE003039.

Mellon, M. T., et al. (2009), Ground ice at the Phoenix landing site: Stability state and origin, *J. Geophys. Res.*, *114*, E00E07, doi:10.1029/2009JE003417.

Melosh, H. J. (1989), *Impact Cratering: A Geologic Process*, Oxford Univ. Press, New York.

Mischna, M. A., M. I. Richardson, R. J. Wilson, and D. J. McCleese (2003), On the orbital forcing of Martian water and CO_2 cycles: A general circulation model study with simplified volatile schemes, *J. Geophys. Res.*, *108*(E6), 5062 doi:10.1029/2003JE002051.

Moore, H. J. (1985), The Martian dust storm of Sol 1742, *J. Geophys. Res.*, *90*, D163–D174.

Morgenstern, A., E. Hauber, D. Reiss, S. van Gasselt, G. Grosse, and L. Schirrmeister (2007), Deposition and degradation of a volatile-rich layer in Utopia Planitia and implications for climate history of Mars, *J. Geophys. Res.*, *112*, E06010, doi:10.1029/2006JE002869.

Mouginot, J., A. Pommerol, W. Kofman, P. Beck, B. Schmitt, A. Herique, C. Grima, A. Safaeinili, and J. J. Plaut (2010), The 3–5 MHz global reflectivity map of Mars by MARSIS/Mars Express: Implications for the current inventory of subsurface H_2O, *Icarus*, *210*, 612–625.

Murchie, S., et al. (2007), Compact Reconnaissance Imaging Spectrometer for Mars (CRISM) on Mars Reconnaissance Orbiter (MRO), *J. Geophys. Res.*, *112*, E05S03, doi:10.1029/2006JE002682.

Mustard, J. F., C. D. Cooper, and M. K. Rifkin (2001), Evidence for recent climate change on Mars from the identification of youthful near-surface ground ice, *Nature*, *412*, 411–414.

Neukum, G., et al. (2004), HRSC: The high resolution stereo camera of Mars Express, *Eur. Space Agency Spec. Publ. ESA*, *SP-1240*, 17–35.

Plaut, J. J., et al. (2007), Subsurface rader sounding of the South Polar Layered Deposits of Mars, *Science*, *316*, 92–95.

Plaut, J. J., A. Safaeinili, J. W. Holt, R. J. Phillips, J. W. Head, R. Seu, N. E. Putzig, and A. Frigeri (2009), Radar evidence for ice in lobate debris aprons in the mid-northern latitudes of Mars, *Geophys. Res. Lett.*, *36*, L02203, doi:10.1029/2008GL036379.

Prettyman, T. H., et al. (2004), Composition and structure of the Martian surface at high southern latitudes from neutron spectroscopy, *J. Geophys. Res.*, *109*, E05001, doi:10.1029/2003JE002139.

Putzig, N. E., and M. T. Mellon (2007), Apparent thermal inertia and the surface heterogeneity of Mars, *Icarus*, *191*, 68–94.

Rempel, A. W. (2007), Formation of ice lenses and frost heave, *J. Geophys. Res.*, *112*, F02S21, doi:10.1029/2006JF000525.

Reufer, A., N. Thomas, W. Benz, S. Byrne, V. Bray, C. Dundas, and M. Searls (2010), Models of high-velocity impacts into dust-covered ice: Application to Martian northern lowlands, *Planet. Space Sci.*, *58*, 1160–1168.

Ruff, S. W., and P. R. Christensen (2002), Bright and dark regions on Mars: Particle size and mineralogical characteristics based on Thermal Emission Spectrometer data, *J. Geophys. Res.*, *107*(E12), 5119, doi:10.1029/2001JE001580.

Schorghofer, N. (2007), Dynamics of ice ages on Mars, *Nature*, *449*, 192–195.

Schorghofer, N., and O. Aharonson (2005), Stability and exchange of subsurface ice on Mars, *J. Geophys. Res.*, *110*, E05003, doi:10.1029/2004JE002350.

Schorghofer, N., and F. Forget (2012), History and anatomy of subsurface ice on Mars, *Icarus*, *220*, 1112–1120.

Schultz, P. H., B. Hermalyn, A. Colaprete, K. Ennico, M. Shirley, and W. S. Marshall (2010), The LCROSS cratering experiment, *Science*, *330*, 468–472.

Sizemore, H. G., A. P. Zent, and A. W. Rempel (2013), Initiation and growth of Martian ice lenses, Lunar Planet. Sci. Conf. 44, abstract #1368.

Smith, M. D. (2002), The annual cycle of water vapor on Mars as observed by the Thermal Emission Spectrometer, *J. Geophys. Res.*, *107*(E11), 5115, doi:10.1029/2001JE001522.

Smith, M. D. (2008), Spacecraft observations of the Martian atmosphere, *Ann. Rev. Earth Planet Sci.*, *36*, 191–219.

Smith, D. E., and M. T. Zuber (1998), The relationship between MOLA northern hemisphere topography and the 6.1-mbar atmospheric pressure surface of Mars, *Geophys. Res. Lett.*, *25*, 4397–4400.

Smith, M. D., M. J. Wolff, R. T. Clancy, and S. L. Murchie (2009a), Compact Reconnaissance Imaging Spectrometer observations of water vapor and carbon monoxide, *J. Geophys. Res.*, *114*, E00D03, doi:10.1029/2008JE003288.

Smith, P. H., et al. (2009b), H_2O at the Phoenix landing site, *Science*, *325*, 58–61. Includes supplementary online material.

Smith, M. D., M. J. Wolff, R. T. Clancy, and the CRISM team (2011), Vertical distribution of aerosols and water vapor using CRISM limb observations, AGU fall meeting, abstract #P24A-08.

Wolkenberg, P., M. D. Smith, V. Formisano, and G. Sindoni (2011), Comparison of PFS and TES observations of temperature and water vapor in the Martian atmosphere, *Icarus*, *215*, 628–638.

Zent, A. P., M. H. Hecht, D. R. Cobos, S. E. Wood, T. L. Hudson, S. M. Milkovich, L. P. DeFlores, and M. T. Mellon (2010), Initial results from the thermal and electrical conductivity probe (TECP) on Phoenix, *J. Geophys. Res.*, *115*, E00E14, doi:10.1029/2009JE003420.

Zuber, M. T., R. J. Phillips, J. C. Andrews-Hanna, S. W. Asmar, A. S. Konopliv, F. G. Lemoine, J. J. Plaut, D. E. Smith, and S. E. Smrekar (2007), Density of Mars' South Polar Layered Deposits, *Science*, *317*, 1718–1719.